Thin-Film Architectures with High Spectral Selectivity for Thermophotovoltaic Cells

Tobias Burger[1], Dejiu Fan[2], Kyusang Lee[3], Stephen R. Forrest[2], and Andrej Lenert[1,*]

[1]Department of Chemical Engineering, University of Michigan, Ann Arbor, MI 48109, USA
[2]Department of Electrical Engineering and Computer Science, Physics, and Materials Science and Engineering, University of Michigan, Ann Arbor, MI 48109, USA
[3]Department of Electrical & Computer Engineering, and Materials Science & Engineering, University of Virginia, Charlottesville, VA 22903, USA

KEYWORDS: thermophotovoltaics (TPV), spectral control, thin film, epitaxial lift-off, combined heat and power (CHP).

ABSTRACT: Thermophotovoltaic (TPV) systems are a promising technology for distributed conversion of high-temperature heat to electricity. To achieve high conversion efficiency, the transport of sub-bandgap radiation between the thermal emitter and PV cell should be suppressed. This can be achieved by recycling sub-bandgap radiation back to the emitter using a spectrally-selective cell. However, conventional TPV cells exhibit limited sub-bandgap reflectance. Here we demonstrate thin-film $In_{0.53}Ga_{0.47}As$ structures with high spectral selectivity, including record-high average sub-bandgap reflectance (96%). Selectivity is enabled by short optical paths through a high-quality material fabricated using epitaxial lift-off, highly-reflective back surfaces, and optimized interference. In addition, we use a parallel-plate TPV model to evaluate the impact of specific structural features on performance and to optimize the cell architecture. We show that a dielectric spacer between InGaAs and the Au back contact is an important feature that enables a predicted TPV efficiency above 50% (with a power output of 2.1 W/cm^2), significantly higher than current TPV devices. This work provides guidelines for the design of high-efficiency, low-cost TPV generators.

Thermophotovoltaic (TPV) systems are a promising alternative to turbines for small-scale energy conversion (~1 kW) such as distributed co-generation of heat and power.[1-4] The technology also has the potential for integration with high-temperature thermal energy storage, a technique that could help regulate power supply.[5-8] A thermophotovoltaic cell generates electricity by converting photons radiated by a hot thermal emitter (Figure 1a).[1] Selective radiative transfer – specifically suppression of sub-bandgap radiative transfer – is essential for high efficiency.[3,6,9-14] However, conventional TPV cells, in which the growth substrate is used in the device, have limited spectral selectivity.[10-12,15] Here, we investigate thin-film TPV cells fabricated using epitaxial lift-off to enable selective radiative transfer and high efficiency. A significant enhancement in spectral selectivity, relative to conventional TPVs, was measured in thin-film $In_{0.53}Ga_{0.47}As$ (hereafter InGaAs) structures because of the reduced optical path and optimized interference. Beyond their optical advantages over conventional TPVs, thin-film devices fabricated using epitaxial lift-off have the potential to increase the external luminescent efficiency[14] and to reduce the cost of TPV generators by reusing expensive III-V substrates.[1,3,12,16-18]

Our work builds on past techniques for enhanced spectral selectivity that can be broadly categorized as either emission control or absorption control.[9-11,15,19-23] Several studies have utilized nanophotonic emitters to selectively emit radiation above the PV cell bandgap.[20-24] However, reduced selectivity at high operating temperatures limits the effectiveness of this emission control strategy.[25-31] Furthermore, the long-term thermal stability of nanostructured emitters has yet to be addressed. Alternatively, PV cells exhibiting selective absorption have facilitated recycling of low-energy photons, and consequently, improved efficiency.[9-11,15] This approach makes use of a cell with a back surface reflector (BSR) or a front surface filter (FSF) to reflect radiation with energy lower than the semiconductor bandgap, while absorbing radiation with higher energies.[9-11,15] Low-energy photons reflected by the cell are re-absorbed by the thermal emitter, decreasing net heat transfer between the emitter and cell (Q_h) without decreasing output power (P_{out}) (Figure 1a). An early demonstration of selective absorption in a Si cell with a Ag BSR reached a thermal-to-electrical conversion efficiency of 26% for an emitter temperature of 2300 K.[15] Utilization of lower bandgap cells has enabled similar efficiencies at moderate temperatures. Siergiej, *et al.* utilized a 0.6 eV InGaAs cell with a Si_3N_4/Au BSR to achieve an efficiency of 20.6% for a 1330 K emitter.[10] Deposition of a dielectric spacer layer on the BSR helps to mitigate sub-bandgap absorption by limiting the intensity of radiation at the absorbing metallic surface.[32-34] This device was later modified to include a FSF, increasing its efficiency to 23.6%.[11] The measured spectral selectivity of these approaches, however, has been limited by absorption of sub-bandgap radiation due to a variety of

possible mechanisms including parasitic absorption in the growth substrate.[10-12,15] There has been only one demonstration of a thin-film TPV device, an InGaAsSb cell with a SiO_x spacer and a Au BSR.[34] However, the destructive substrate removal process used to fabricate this device makes it incompatible with wafer reuse. Further, the device exhibits limited spectral selectivity, speculated to be the result of sub-bandgap absorption by macro-scale defects resulting from substrate removal.

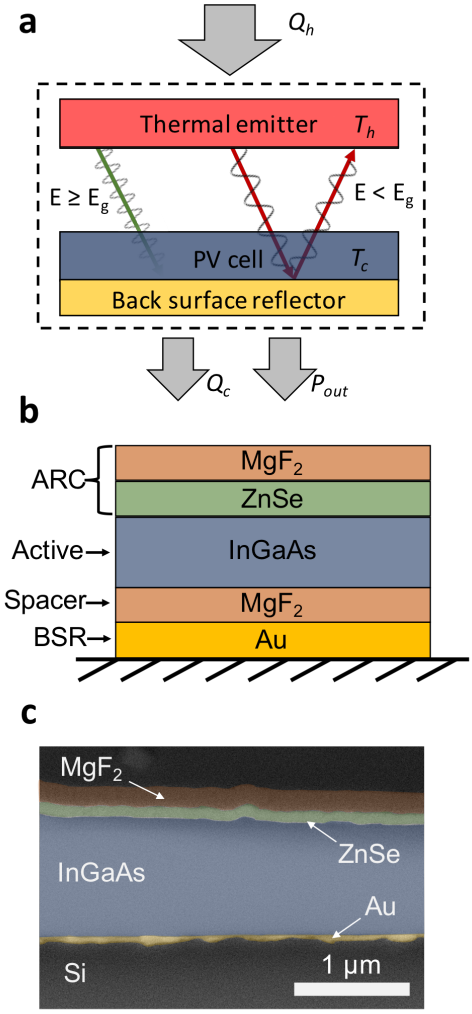

Figure 1. a) Energy flows in a parallel plate TPV system with sub-bandgap photon recycle. Spectrally selective absorption is achieved in a thin-film cell, decreasing waste heat (Q_c) and net heat transfer between the emitter and cell (Q_h), without decreasing output power (P_{out}). b) General schematic of the thin-film structures considered here, which include an InGaAs active layer and combinations of the following layers: back surface reflector (BSR), anti-reflection coating (ARC), and dielectric back spacer. c) Cross-sectional SEM image of an example structure (false-colored). From top to bottom: 190 nm MgF_2 (orange), 110 nm ZnSe (green), 1.3 μm InGaAs (blue), 400 nm Au BSR (yellow), Si handle (gray).

Our fabricated structures exhibit higher reflectance below the semiconductor bandgap than previous TPVs, coupled with high absorption of radiation above the bandgap. To evaluate the impact of specific thin-film structural features on performance and to optimize the cell architecture, we use a prediction of TPV performance in a parallel-plate geometry. Our work provides design guidelines for selectively-absorptive, high-efficiency thin-film TPVs.

RESULTS AND DISCUSSION

Optical Properties of Thin InGaAs-based Structures. In this section, we identify techniques for enhancing the spectral selectivity of fabricated thin films. We also compare the measured reflectance to optical modeling based on the transfer matrix method.[35,36]

As a baseline structure, we fabricated and characterized the optical properties of a 1.38 μm thick epitaxial layer of InGaAs on a Au BSR, hereafter called *BSR* (Figure 2a). A 4 nm AlAs sacrificial layer was grown by molecular beam epitaxy on a (100) InP wafer, followed by the InGaAs epitaxial layer. The thin film was cold-weld bonded to a Au-coated Si wafer handle and removed from the InP wafer by epitaxial lift-off. The absorptance (a) of the *BSR* structure, as a function of incident photon energy (E) and incidence angle (θ), is compared to the experimental response measured by a Fourier transform infrared (FT-IR) microscope (Figure 2a). The response is characterized by selective absorptance above the material bandgap. Average, weighted optical properties were calculated with respect to the photon flux of a 1500 K emitter. The measured response exhibits an average absorptance of 61% above the bandgap and 5.5% below the bandgap (94.5% average sub-bandgap reflectance).

To enhance the above-bandgap absorption of the structure, we deposited a double layer anti-reflection coating (ARC) (190 nm MgF_2, 110 nm ZnSe) on a 1.3 μm InGaAs layer with a Au BSR, hereafter called *ARC*. The optical response is characterized by a pronounced increase in absorptance above the bandgap compared to the *BSR* structure and a reduction of peak-to-peak absorptance variations (Figure 2b). On average, the *ARC* structure exhibits absorptance of 81% above the bandgap and 5.3% absorptance below the bandgap (94.7% average sub-bandgap reflectance). A parasitic absorptance peak is observed at 0.44 eV, which is attributed to absorption in the double-layer ARC, as confirmed by measurement of the ARC directly on Au (details provided in Supporting Information).

As a strategy for enhancing sub-bandgap reflectance, we fabricated a different structure, consisting of a 430 nm thick MgF_2 spacer between a 2.1 μm thick InGaAs layer and Au BSR. The InGaAs-MgF_2-Au structure, hereafter called *Spacer,* exhibits an average sub-bandgap reflectance of 95.7% (Figure 2c), better than either of the previous structures. A parasitic absorptance peak at 0.44 eV, similar to the one observed in the *ARC* structure, parly limits the desired reflectance. The *Spacer* structure exhibits above-bandgap absorptance of 62.5%, comparable to that of *BSR* structure.

Outside of the parasitic peak, the simulated optical response of each of the architectures agrees with its measured response within 9% above the bandgap and 5% below the bandgap. The model also captures the observed oscillatory interference variations in

absorptance. Material optical properties obtained from literature were used in the simulations (see Supporting Information).[37-43] All experimental layer thicknesses are estimated from their growth rate during fabrication; fine thickness adjustments (< 10% of layer thickness), within the range of uncertainty from the growth rate estimation, were made using a least squares regression between the simulated and experimental optical response.

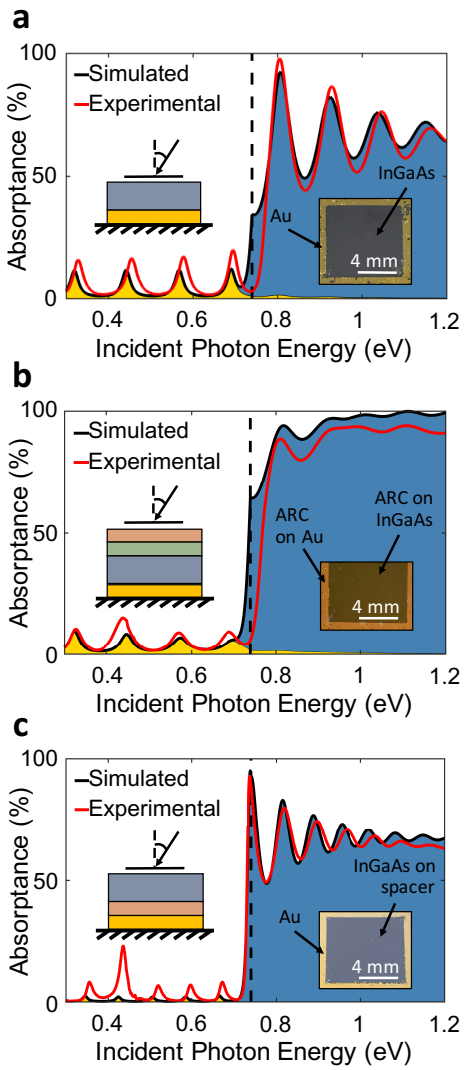

Figure 2. Simulated (red) and measured (black) optical responses of the (a) *BSR* structure, (b) *ARC* structure, (c) *Spacer* structure. Blue (yellow) shading indicates predicted absorption by the InGaAs (Au) layer. Left inset: Angle of incidence (15°). Right inset: Photograph of structure.

Evaluating Strategies for Enhanced Selectivity. To evaluate the spectral selectivity of the three cases (*BSR*, *ARC*, and *Spacer*), we use a prediction of TPV performance based on the optical response and geometry of the cell, operating at 20°C, in perfect view of a high-temperature black emitter (see **Energy Conversion Simulation**). For a fair comparison among cases, we varied the layer thicknesses within the constraints of the three cases to maximize the predicted conversion efficiency (Equation 9). The performance of the optimized structures (Table 1) is compared with an InGaAs cell without a BSR (hereafter called *Blackbody*), characterized by no spectral selectivity. We set the thickness of the InGaAs layer in the *Blackbody* case to twice that of the *BSR* case, such that the optical path lengths through InGaAs are approximately equal (assuming wavevectors within the active layer are near-normal because of the high refractive index of InGaAs relative to vacuum).[12,16]

A significant enhancement in efficiency, relative to the blackbody case, is predicted for cells with a reflective back surface – suggesting it is an essential feature for achieving high efficiency. For example, the *BSR* case is predicted to achieve 43% efficiency when paired with a 1500 K emitter, whereas the *Blackbody* case achieves only 8% efficiency under these conditions (Table 1). Use of a MgF_2 back spacer increases this efficiency gain further. The *Spacer* case is predicted to exhibit 8% greater (absolute) efficiency than the *BSR* case because of its higher sub-bandgap reflectance (98.9% vs. 96.8%).

An anti-reflection coating, on the other hand, is less important for improving efficiency. However, an ARC considerably improves the above-bandgap absorptance and, consequently, the power density. For example, the *ARC* case exhibits ~0.8 W/cm^2 higher power density than either the *BSR* or the *Spacer* case (Figure 3b).

Structure Optimization. To optimize the overall cell architecture, we modeled a TPV cell with an ARC *and* a spacer (Figure 3a inset), hereafter called the *Combined* case. The optimized *Combined* case exhibits high spectral selectivity (Figure 3a), achieving higher above-bandgap absorptance than the *Spacer* case without significantly compromising sub-bandgap reflectance (Table 1). Because of its superior optical properties, the *Combined* case is predicted to operate with higher efficiency than either the *BSR* or *Spacer* case (Figure 3b) and with a power output approaching that of the *ARC* case (Figure 3c). Specifically, for an optimized *Combined* cell, we predict an efficiency of 52% and a power output of 2.1 W/cm^2 when paired with a 1500 K black emitter.

Our simulation suggests that spacers are an important feature of high-efficiency thin-film InGaAs cells. Spacers limit parasitic absorption by the metal contact by reducing the intensity that reaches the back interface. Provided that parasitic absorption is mitigated in the active layers, average sub-bandgap reflectance approaching 99% may be achieved with the use of a back spacer. Development of a TPV device with a back spacer will require the design of electrical contacts capable of collecting charge carriers laterally or across this dielectric region. Prior demonstration of a TPV device with dielectric claddings (ARC and spacer) utilized monolithic series interconnections to electrically contact the active region.[34] Similar design elements may be appropriate for developing TPV modules with the proposed MgF_2 spacer.

Our study identified that the optimal InGaAs thickness depends on the case. Thinner active layers (1-1.5 μm) are optimal when using back spacers, which may also reduce processing costs. We speculate that the optimum thickness is observed in this range because ultra-thin TPV cells (<300 nm) suffer from low photo-generation while thicker devices exhibit increased rates of non-radiative recombination and higher parasitic sub-bandgap absorption.

Table 1. Optimized architecture and performance for several InGaAs structures (T_h = 1500 K).

	MgF_2 [μm]	ZnSe [μm]	InGaAs [μm]	MgF_2 [μm]	Back surface	$\bar{a}(E \geq E_g)$ [%]	$\bar{a}(E < E_g)$ [%]	η [%]	P_{out} [W cm^{-2}]
BSR	-	-	0.97	-	Au	60.8	3.2	42.9	1.52
ARC	0.20	0.10	2.78	-	Au	92.2	3.7	44.6	2.27
Spacer	-	-	1.1	0.44	Au	61.1	1.1	51.0	1.52
Combined	0.46	0.15	1.46	0.42	Au	82.3	1.4	51.7	2.07
Blackbody	*	*	1.93	-	Black	100	100	8.1	2.32

*The hypothetical *Blackbody* case is assumed to have perfect broadband absorptance.

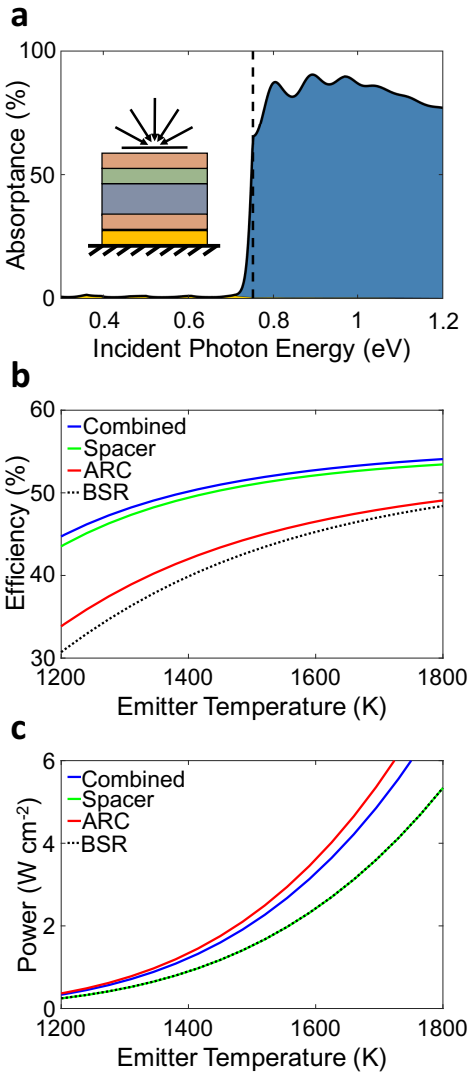

Figure 3. a) Calculated, hemispherically-averaged optical response of the *Combined* structure. Blue and yellow shading indicates specific absorption by the InGaAs and Au layer, respectively. Inset: Structure schematic. Comparison of predicted (b) efficiency, (c) power output for each case, optimized given its discrete set of layers.

CONCLUSION

In summary, we demonstrated high spectral selectivity in thin-film structures by using back surface reflectors and by optimizing interference. Specifically, we fabricated thin-film structures with record high average sub-bandgap reflectance (96%). We identified that reflective back surfaces are the most important feature for high efficiency cells. The enhanced reflectance due to a dielectric spacer layer, between the InGaAs and the Au back contact, results in predicted TPV efficiencies above 50% for a 1500 K black emitter. When combined with a double-layer anti-reflection coating, high power densities (~2 W/cm^2) are also achievable. The potential for a dramatic increase of conversion efficiency through improved spectral selectivity, combined with the potential for reduced module costs through wafer reuse, supports the prospect of thin-film TPVs for applications in distributed power generation. Beyond the high spectral selectivity demonstrated here, development of high-performance thin-film TPV systems will require precise doping of active materials and design of selective electrical contacts with low parasitic absorption.

EXPERIMENTAL SECTION

InGaAs Film Growth. InGaAs structures were grown by gas-source molecular beam epitaxy. A 200 nm thick, unintentionally doped InP buffer layer was grown on a 2 inch diameter, Zn doped (100) InP wafer, followed by a 4 nm thick AlAs sacrificial layer, and an unintentionally doped i-InGaAs absorption layer. The wafer was then diced into 6 mm x 6 mm squares using an ADT7100 dicing saw. Samples were rinsed with DI water for 30 seconds to remove dicing residue and stored in acetone to prevent surface contamination. Immediately before further processing, samples were soaked in buffered HF for 1 minute and rinsed in DI water for 10 seconds to remove surface native oxides.

InGaAs with BSR Fabrication. Following InGaAs film growth, a 200 nm thick Au layer was deposited by electron beam evaporation on the epitaxial InGaAs surface. A 500 μm thick (100) B doped Si wafer was immersed in buffered HF for 1 minute and rinsed in DI water for 10 seconds to remove native oxides. A 5 nm thick Ir adhesion layer and a 200 nm thick Au layer were deposited on the Si wafer. The metalized surfaces of the sample and wafer were cold-weld bonded by applying heat (200°C) and pressure (5 MPa) for 5 minutes under vacuum (10^{-4} mTorr) using an EVG 520 wafer bonder. The epitaxial layers were lifted off from the parent InP wafer by removing the AlAs layer through immersion in 17% HF at 45°C with 400 rpm agitation by magnetic stir bar for 1.5 hours. Following lift-off, samples were stored at 60°C in Remover PG (MicroChem) to prevent oxide formation on the epitaxial surface prior to further processing.

ARC Fabrication. Following InGaAs with BSR fabrication, a ZnSe/MgF_2 bilayer anti-reflection coating was deposited onto the epitaxial InGaAs surface by electron beam evaporation.

InGaAs with Back Spacer Fabrication. Following InGaAs film growth, a 200 nm thick Au layer was deposited by electron beam evaporation on the epitaxial InGaAs surface. Similarly, a 5 nm thick Ir adhesion layer and a 200 nm thick Au layer were deposited on a 25 μm thick E-type Kapton foil substrate. The metalized surfaces of the sample and foil were cold-weld bonded by applying heat (200°C) and pressure (5 MPa) for 5 minutes under vacuum (10^{-4} mTorr) using an EVG 520 wafer bonder. The epitaxial layers were lifted off from the parent InP wafer by removing the AlAs layer through immersion in 17% HF at 45°C with 400 rpm agitation by magnetic stir bar for 1.5 hours. Following lift-off by HF etch, MgF_2 was deposited onto the epitaxial InGaAs surface by electron beam evaporation, followed by a 200 nm thick Au layer. A 500 μm thick (100) B doped Si wafer was immersed in buffered HF for 1 minute and rinsed in DI water for 10 seconds to remove native oxides. A 5 nm thick Ir adhesion layer and a 200 nm thick Au layer were deposited on the Si wafer. The metalized surfaces of the sample and Si wafer were cold-weld bonded by applying heat (200°C) and pressure (5 MPa) for 5 minutes under vacuum (10^{-4} mTorr) using an EVG 520 wafer bonder. The Kapton host foil was removed by inductively coupled plasma (ICP) reactive-ion etching (RIE) (Oxford Plasmalab System 100) with 20 sccm of O_2 at a chamber pressure of 6 mTorr, stage temperature of 0°C, ICP power of 500 W, and forward power of 100 W for 25 minutes. The remaining Ir and Au layers were removed using ICP RIE with 12:9:5 sccm of H_2:Cl_2:Ar at a chamber pressure of 10 mTorr, stage temperature of 0°C, ICP power of 500 W, and forward power of 100 W for 2.5 minutes.

Energy Conversion Simulation. During TPV operation (Figure 1a), input heat (Q_h) increases the temperature of the emitter (T_h) and drives thermal emission (Q_{emit}). The photon flux of an emitting blackbody, Φ, as a function of emitted photon energy, E, is calculated via Planck's Law:

$$\Phi(E) = \frac{2\pi E^2}{c^2 h^3 \left(\exp\left(\frac{E}{k_B T}\right)-1\right)} \quad (1)$$

where c is the speed of light, h is Planck's constant, and k_B is the Boltzmann constant. Radiation emitted by the thermal emitter, $\Phi_h(E)$, is described by Planck's Law evaluated at T_h.

A portion of incident radiation is absorbed by the PV cell and the rest is reflected (Q_{ref}). Hemispherically-averaged absorptance ($a(E)$) is calculated by integration of the angle-dependent absorption spectrum ($a(E,\theta)$) over angles (θ,ϕ):

$$a(E) = \frac{\int_0^{2\pi}\int_0^{\pi/2} a(E,\theta)\cos(\theta)\sin(\theta)d\theta d\phi}{\int_0^{2\pi}\int_0^{\pi/2} \cos(\theta)\sin(\theta)d\theta d\phi} \quad (2)$$

Upon absorption in the InGaAs layer, above-bandgap photons generate excited electron-hole pairs, enabling the generation of electrical power (P_{out}).

The maximum short circuit current, is calculated from the angle-averaged optical response, $a(E)$, and the emitted photon flux, $\Phi_h(E)$:

$$J_{SC} = q\int_{E_g}^{\infty} a(E)\Phi_h(E)dE \quad (3)$$

where q is the elementary charge of an electron and E_g is the bandgap.

The photocurrent, J, as a function of voltage across the cell, V, is the difference between the short circuit current and recombination loss, given by:

$$J(V) = J_{sc} - q\left(R_{rad} + R_{SRH} + R_{Aug}\right) \quad (4)$$

where R_{rad}, R_{SRH}, and R_{Aug}, are the radiative, Shockley-Reed-Hall (SRH), and Auger recombination rates, respectively. The radiative recombination rate is:

$$R_{rad} = exp\left(\frac{qV}{k_B T_c}\right)\int_{E_g}^{\infty} a(E)\Phi_c(E)dE \quad (5)$$

In the case of low semiconductor doping concentration (N_D), such that the injected carrier concentration (n_o) is greater than N_D, the non-radiative recombination rates are independent of dopant concentration.[44] In this high-injection regime, the non-radiative SRH recombination rate is:

$$R_{SRH} = \frac{Ln_i^2}{\tau_{SRH}} exp\left(\frac{qV}{2k_B T_c}\right) \quad (6)$$

where L is the thickness of the active region, τ_{SRH} is the SRH recombination lifetime, and n_i is the intrinsic carrier concentration. Literature values of intrinsic carrier concentration and SRH lifetime for InGaAs at 300 K are $6.3\text{x}10^{11}$ cm^{-3} and 47.4 μs, respectively.[45,46] The non-radiative, Auger recombination rate, R_{Aug}, is:

$$R_{Aug} = L\left(C_n + C_p\right) n_i^3 exp\left(\frac{3qV}{2k_B T_c}\right) \quad (7)$$

where C_n and C_p are the Auger recombination coefficients for recombination involving two electrons and two holes, respectively. The Auger recombination coefficients are $C_n = C_p = 8.1\text{x}10^{-29}$ cm^{-3}.[46]

The output power of the cell is the product of the photocurrent and the voltage:

$$P_{out} = J(V)\cdot V \quad (8)$$

Efficiency is calculated from the maximum power point voltage, V_{MPP}, and current response, J_{MPP} via:

$$\eta_{TPV} = \frac{P_{out}}{Q_h} = \frac{P_{out}}{Q_{emit} - Q_{ref}}$$

$$= \frac{J_{MPP}\cdot V_{MPP}}{\int_0^{\infty} E\cdot\Phi_h(E)dE - \int_0^{\infty}(1-a(E))\cdot E\cdot\Phi_h(E)dE} \quad (9)$$

ASSOCIATED CONTENT

Supporting Information

The Supporting Information is available free of charge on the ACS Publications website.

Optical properties of InGaAs, Au, MgF_2, and ZnSe (Figure S1). Sub-bandgap, parasitic absorption in bilayer ARC (Figure S2). Predicted, hemispherically-averaged absorptance of the optimized *BSR, ARC,* and *Spacer* cases (Figure S3). SEM image of InGaAs-Au interface (Figure S4) Comparison of predicted performance to the radiative limit (Figure S5). (PDF).

AUTHOR INFORMATION

Corresponding Author

*E-mail: alenert@umich.edu

Funding Sources

This material is based upon work supported by the National Science Foundation under Grant No. IIP-1820395.

REFERENCES

(1) Coutts, T. J. Overview of Thermophotovoltaic Generation of Electricity. *Sol. Energy Mater. Sol. Cells* **2001**, *66* (1-4), 443-452.

(2) Bianchi, M.; Ferrari, C.; Melino, F.; Peretto, A. Feasibility Study of a Thermo-Photo-Voltaic System for CHP Application in Residential Buildings. *Appl. Energy* **2012**, *97* (x), 704-713.

(3) Durisch, W.; Bitnar, B. Novel Thin Film Thermophotovoltaic System. *Sol. Energy Mater. Sol. Cells* **2010**, *94* (6), 960-965.

(4) Fraas, L. M.; Avery, J. E.; Huang, H. X. Thermophotovoltaic Furnace-Generator for the Home Using Low Bandgap GaSb Cells. *Semicond. Sci. Technol.* **2003**, *18* (5), 247-253.

(5) Amy, C.; Budenstein, D.; Bagepalli, M.; England, D.; Deangelis, F.; Wilk, G.; Jarrett, C.; Kelsall, C.; Hirschey, J.; Wen, H.; et al. Pumping Liquid Metal at High Temperatures up to 1,673 Kelvin. *Nature* **2017**, *550* (7675), 199-203.

(6) Seyf, H. R.; Henry, A. Thermophotovoltaics: A Potential Pathway to High Efficiency Concentrated Solar Power. *Energy Environ. Sci. Energy Environ. Sci* **2016**, *9* (9), 2654-2665.

(7) Datas, A.; Chubb, D. L.; Veeraragavan, A. Steady State Analysis of a Storage Integrated Solar Thermophotovoltaic (SISTPV) System. *Sol. Energy* **2013**, *96*, 33-45.

(8) Datas, A.; Ramos, A.; Martí, A.; del Cañizo, C.; Luque, A. Ultra High Temperature Latent Heat Energy Storage and Thermophotovoltaic Energy Conversion. *Energy* **2016**, *107*, 542-549.

(9) Bitnar, B. Silicon, Germanium and Silicon/germanium Photocells for Thermophotovoltaics Applications. *Semicond. Sci. Technol.* **2003**, *18* (5), S221.

(10) Siergiej, R. R.; Wernsman, B.; Derry, S. A.; Mahorter, R. G.; Wehrer, R. J.; Link, S. D.; Palmisiano, M. N.; Messham, R. L.; Murray, S.; Murray, C. S.; et al. 20% Efficient InGaAs/InPAs TPV Cells. In *Thermophotovoltaic Generation of Electricity 5th Conference*; 2003; pp 414-423.

(11) Wernsman, B.; Siergiej, R. R.; Link, S. D.; Mahorter, R. G.; Palmisiano, M. N.; Wehrer, R. J.; Schultz, R. W.; Schmuck, G. P.; Messham, R. L.; Murray, S.; et al. Greater than 20% Radiant Heat Conversion Efficiency of a Thermophotovoltaic Radiator/module System Using Reflective Spectral Control. *IEEE Trans. Electron Devices* **2004**, *51* (3), 512-515.

(12) Ganapati, V.; Xiao, T. P.; Yablonovitch, E. Ultra-Efficient Thermophotovoltaics Exploiting Spectral Filtering by the Photovoltaic Band-Edge arXiv: 1611 . 03544v2 [Physics . Optics] 7 Feb 2018. **2018**, 1-14.

(13) Lenert, A.; Nam, Y.; Bierman, D. M.; Wang, E. N. Role of Spectral Non-Idealities in the Design of Solar Thermophotovoltaics. *Opt. Express* **2014**, *22* (S6), A1604.

(14) Miller, O. D.; Yablonovitch, E.; Kurtz, S. R. Strong Internal and External Luminescence as Solar Cells Approach the Shockley-Queisser Limit. *IEEE J. Photovoltaics* **2012**, *2* (3), 303-311.

(15) Swanson, R. M. Silicon Photovoltaic Cells in Thermophotovoltaic Energy Conversion. *Int. Electron Devices Meet.* **1978**, 70-73.

(16) Jurczak, P.; Onno, A.; Sablon, K.; Liu, H. Efficiency of GaInAs Thermophotovoltaic Cells: The Effects of Incident Radiation, Light Trapping and Recombinations. *Opt. Express* **2015**, *23* (19), A1208.

(17) Lee, K.; Zimmerman, J. D.; Hughes, T. W.; Forrest, S. R. Non-Destructive Wafer Recycling for Low-Cost Thin-Film Flexible Optoelectronics. *Adv. Funct. Mater.* **2014**, *24* (27), 4284-4291.

(18) Lee, K.; Lee, J.; Mazor, B. A.; Forrest, S. R. Transforming the Cost of Solar-to-Electrical Energy Conversion: Integrating Thin-Film GaAs Solar Cells with Non-Tracking Mini-Concentrators. *Light Sci. Appl.* **2015**, *4* (5), e288.

(19) Fourspring, P. M.; Depoy, D. M.; Rahmlow, T. D.; Lazo-wasem, J. E.; Gratrix, E. J. Optical Coatings for Thermophotovoltaic Spectral Control. **2006**, No. 1, 1-3.

(20) Lenert, A.; Bierman, D. M.; Nam, Y.; Chan, W. R.; Celanović, I.; Soljačić, M.; Wang, E. N. A Nanophotonic Solar Thermophotovoltaic Device. *Nat. Nanotechnol.* **2014**, *9* (9), 126-130.

(21) Bierman, D. M.; Lenert, A.; Chan, W. R.; Bhatia, B.; Celanović, I.; Soljačić, M.; Wang, E. N. Enhanced Photovoltaic Energy Conversion Using Thermally Based Spectral Shaping. *Nat. Energy* **2016**, *1* (6), 16068.

(22) Shimizu, M.; Kohiyama, A.; Yugami, H. High-Efficiency Solar-Thermophotovoltaic System Equipped with a Monolithic Planar Selective Absorber/emitter. *J. Photonics Energy* **2015**, *5* (1), 53099.

(23) Arpin, K. A.; Losego, M. D.; Braun, P. V. Electrodeposited 3D Tungsten Photonic Crystals with Enhanced Thermal Stability. *Chem. Mater.* **2011**, *23* (21), 4783-4788.

(24) Chan, W. R.; Bermel, P.; Pilawa-Podgurski, R. C. N.; Marton, C. H.; Jensen, K. F.; Senkevich, J. J.; Joannopoulos, J. D.; Soljacic, M.; Celanovic, I. Toward High-Energy-Density, High-Efficiency, and Moderate-Temperature Chip-Scale Thermophotovoltaics. *Proc. Natl. Acad. Sci. U. S. A.* **2013**, *110* (14), 5300-5314.

(25) Nam, Y.; Yeng, Y. X.; Lenert, A.; Bermel, P.; Celanović, I.; Soljačić, M.; Wang, E. N. Solar Thermophotovoltaic Energy Conversion Systems with Two-Dimensional Tantalum Photonic Crystal Absorbers and Emitters. *Sol. Energy Mater. Sol. Cells* **2014**, *122*, 287-296.

(26) Chou, J. B.; Yeng, Y. X.; Lee, Y. E.; Lenert, A.; Rinnerbauer, V.; Celanovic, I.; Soljačić, M.; Fang, N. X.; Wang, E. N.; Kim, S.-G. Enabling Ideal Selective Solar Absorption with 2D Metallic Dielectric Photonic Crystals. *Adv. Mater.* **2014**, *26* (47), 8041-8045.

(27) Chou, J. B.; Yeng, Y. X.; Lenert, A.; Rinnerbauer, V.; Celanovic, I.; Soljačić, M.; Wang, E. N.; Kim, S.-G. Design of Wide-Angle Selective Absorbers/emitters with Dielectric Filled Metallic Photonic Crystals for Energy Applications. *Opt. Express* **2014**, *22* (S1), A144.

(28) Rinnerbauer, V.; Lenert, A.; Bierman, D. M.; Yeng, Y. X.; Chan, W. R.; Geil, R. D.; Senkevich, J. J.; Joannopoulos, J. D.; Wang, E. N.; Soljačić, M.; Celanovic, I. Metallic Photonics Crystal Absorber-Emitter for Effiient Spectral Control in High-Temperature Solar Thermophotovoltaics. *Adv. Energy Mater.* **2014**, *4* (12), 1400334.

(29) Yeng, Y. X.; Ghebrebrhan, M.; Bermel, P.; Chan, W. R.; Joannopoulos, J. D.; Soljacic, M.; Celanovic, I. Enabling High-Temperature Nanophotonics for Energy Applications. *Proc. Natl. Acad. Sci.* **2012**, *109* (7), 2280-2285.

(30) Rinnerbauer, V.; Yeng, Y. X.; Chan, W. R.; Senkevich, J. J.; Joannopoulos, J. D.; Soljacic, M.; Celanovic, I. High-Temperature Stability and Selective Thermal Emission of Polycrystalline Tantalum Photonic Crystals. *Opt. Express* **2013**, *21* (9), 11482.

(31) Shimizu, M.; Kohiyama, A.; Yugami, H. Evaluation of Thermal Stability in Spectrally Selective Few-Layer Metallo-Dielectric Structures for Solar Thermophotovoltaics. *J. Quant. Spectrosc. Radiat. Transf.* **2018**, *212*, 45-49.

(32) Wu, X.; Duda, A.; Carapella, J. J.; Ward, J. S.; Webb, J. D.; Wanlass, M. W. A Study of Contacts and Back-Surface Reflectors Interconnected Modules. F*ourth Conf. thermophotovoltaic Gener. Electr* **1998**, *517*.

(33) Clevenger, M. B.; Murray, C. S.; Ringel, S. A.; Sacks, R. N.; Qin, L.; Charache, G. W.; Depoy, D. M. Optical Properties of Thin Semiconductor Device Structures with Reflective Back-Surface Layers. *Fourth NREL Conf. thermophotovoltaic Gener. Electr.* **1999**, 327-334.

(34) Wang, C. a; Shiau, D. a; Murphy, P. G.; O'Brien, P. W.; Huang, R. K.; Connors, M. K.; Anderson, A. C.; Donetsky, D.; Anikeev, S.; Belenky, G.; Depoy, D. M.; Nichols, G. Wafer Bonding and Epitaxial Transfer of GaSb-Based Epitaxy to GaAs for Monolithic Interconnection of Thermophotovoltaic Devices. *J. Electron. Mater.* **2004**, *33* (3), 213-217.

(35) Born, M.; Wolf, E. *Principles of Optics*, 4th ed.; Perfamon Press Ltd., 1970.

(36) Deng, X.-H.; Liu, J.-T.; Yuan, J.-R.; Liao, Q.-H.; Liu, N.-H. A New Transfer Matrix Method to Calculate the Optical Absorption of Graphene at Any Position in Stratified Media. *Europhys. Lett.* **2015**, *109* (2), 27002.

(37) Li, H. H. Refracfive Index of Alkali Halides and Its Wavelength End Temperature Derivatives. *J. Phys. Chem. Ref. Data* **1976**, *5* (2), 3299-528.

(38) Tatian, B. Fitting Refractive-Index Data with the Sellmeier Dispersion Formula. *Appl. Opt.* **1984**, *23* (24), 4477.
(39) Connolly, J.; DiBenedetto, B.; Donadio, R. Specifications Of Raytran Material. In *Proc. SPIE*; Fischer, R. E., Ed.; 1979; pp 141-144.
(40) Palik, E. D. *Handbook of Optical Constants of Solids*; Academic Press, 1998.
(41) Dixon, J. R.; Ellis, J. M. Optical Properties of N-Type Indium Arsenide in the Fundamental Absorption Edge Region. *Phys. Rev.* **1961**, *123* (5), 1560-1566.
(42) Sturge, M. D. Optical Absorption of Gallium Arsenide between 0.6 and 2.75 eV. *Phys. Rev.* **1962**, *127* (3), 768-773.
(43) Olmon, R. L.; Slovick, B.; Johnson, T. W.; Shelton, D.; Oh, S.-H.; Boreman, G. D.; Raschke, M. B. Optical Dielectric Function of Gold. *Phys. Rev. B* **2012**, *86* (23), 235147.
(44) Krier, A. *Mid-Infrared Semiconductor Optoelectronics*; Springer, 2006.
(45) Electrical Properties of Gallium Indium Arsenide (GaInAs) http://www.ioffe.ru/SVA/NSM/Semicond/GaInAs/ebasic.html (accessed Jun 28, 2017).
(46) Ahrenkiel, R. K.; Ellingson, R.; Johnston, S.; Wanlass, M. Recombination Lifetime of In0.53Ga0.47As as a Function of Doping Density. *Appl. Phys. Lett.* **1998**, *72* (26), 3470-3472.

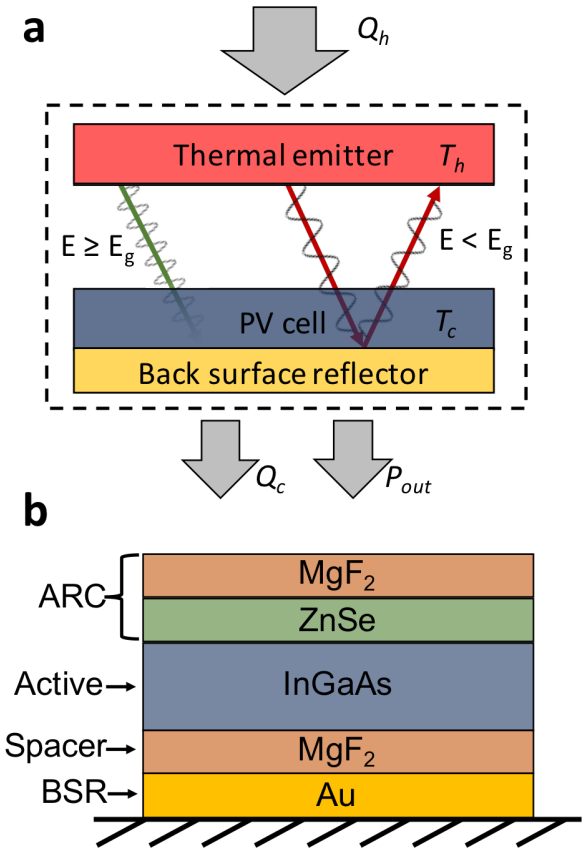
a
Q_h
Thermal emitter T_h
$E \geq E_g$
$E < E_g$
PV cell T_c
Back surface reflector
Q_c
P_{out}
b
ARC
MgF_2
ZnSe
Active
InGaAs
Spacer
MgF_2
BSR
Au
c
MgF_2
ZnSe
InGaAs
Au
Si
1 μm

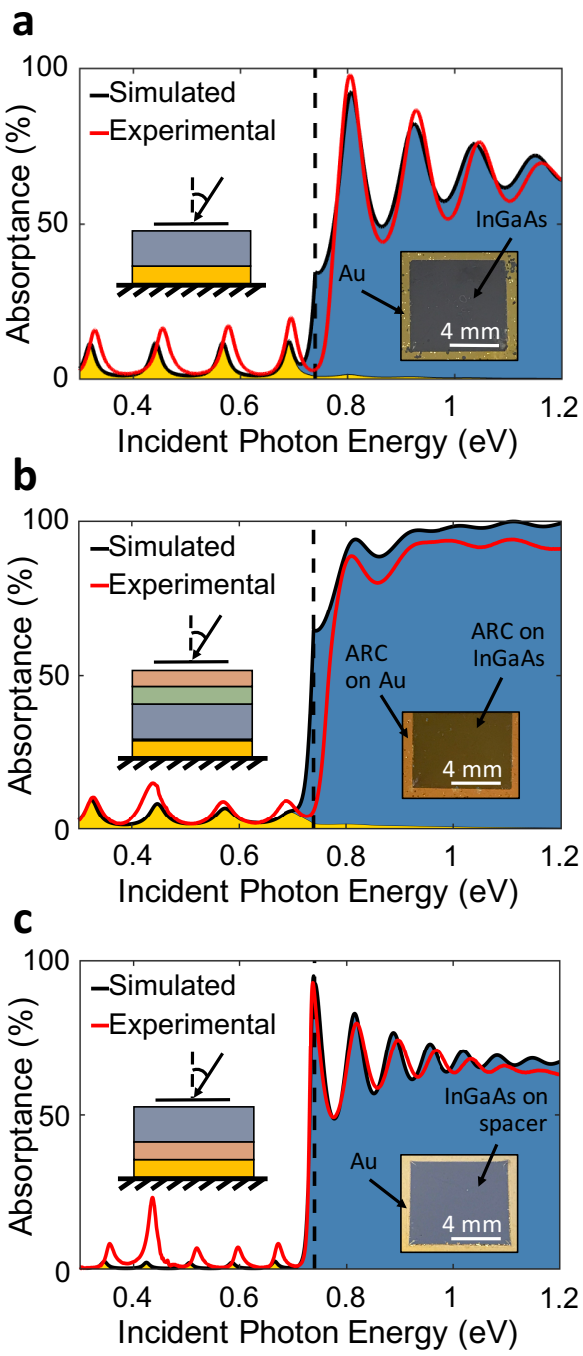
a
100
50
0
Absorptance (%)
Simulated
Experimental
InGaAs
Au
4 mm
0.4
0.6
0.8
1
1.2
Incident Photon Energy (eV)
b
100
50
0
Absorptance (%)
Simulated
Experimental
ARC on InGaAs
ARC on Au
4 mm
0.4
0.6
0.8
1
1.2
Incident Photon Energy (eV)
c
100
50
0
Absorptance (%)
Simulated
Experimental
InGaAs on spacer
Au
4 mm
0.4
0.6
0.8
1
1.2
Incident Photon Energy (eV)

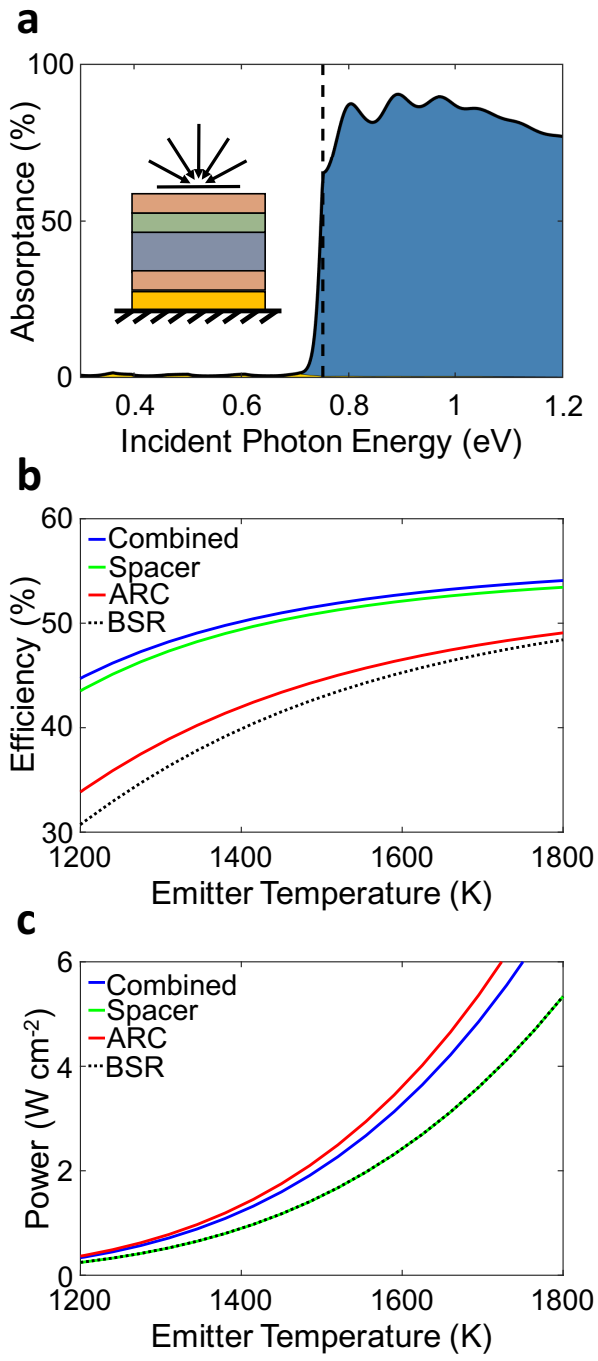
a
100
50
0
Absorptance (%)
0.4
0.6
0.8
1
1.2
Incident Photon Energy (eV)
b
60
50
40
30
Efficiency (%)
Combined
Spacer
ARC
BSR
1200
1400
1600
1800
Emitter Temperature (K)
c
6
4
2
0
Power (W cm-2)
Combined
Spacer
ARC
BSR
1200
1400
1600
1800
Emitter Temperature (K)

Table of contents graphic